SCIENCE CHINA
Physics, Mechanics & Astronomy

• Article •
85th Anniversary for the Institute of Physics, Chinese Academy of Sciences

December 2013 Vol.56 No.12: 2370–2376
doi: 10.1007/s11433-013-5349-1

A study on surface symmetry and interfacial enhancement of $SrTiO_3$ by second harmonic generation

ZHAO RuiQiang, JIN KuiJuan*, GUO HaiZhong, LU HuiBin & YANG GuoZhen

Beijing National Laboratory for Condensed Matter Physics, Institute of Physics, Chinese Academy of Sciences, Beijing 100190, China

Received July 18, 2013; accepted August 26, 2013; published online November 14, 2013

The symmetry of the surfaces of $SrTiO_3$ and slightly Nb-doped $SrTiO_3$ crystals was investigated by the optical reflected second harmonic generation technique. The good agreement between experimental and theoretical results of the second harmonic intensity dependence on the azimuth angle indicates that the $SrTiO_3$ (001) surface is with 4*mm* symmetry and the Nb-doped $SrTiO_3$ (111) surface with 3*m* symmetry. The measurements of the polarization dependent second harmonic intensity confirm that conclusion. The enhancement of the surface polarization in the structure of $SrTiO_3$ capped $La0_{.9}Sr_{0.1}MnO_3$ films compared with that in the $La_{0.9}Sr_{0.1}MnO_3$ films has been obtained.

perovskite oxides, surface, crystal symmetry, second harmonic generation

PACS number(s): 72.80.Ga, 68.35.Bs, 61.50.Ah, 42.65.Ky

Citation: Zhao R Q, Jin K J, Guo H Z, et al. A study on surface symmetry and interfacial enhancement of $SrTiO_3$ by second harmonic generation. Sci China-Phys Mech Astron, 2013, 56: 2370–2376, doi: 10.1007/s11433-013-5349-1

1 Introduction

The surface and interface science of perovskite oxides is a relatively young field that attracts extensive interest due to their rich physical properties [1–3]. Strontium titanate, $SrTiO_3$ (STO), is a model material of a wide class of the transition metal oxides with the perovskite structure, and is also a typical substrate material for the epitaxial growth of tremendous perovskite oxide thin films and heterostructures [4]. Particularly, in recent years STO has received considerable attention especially after the discovery of the two-dimensional electron gas at the interface between the two typical insulators, i.e., $LaAlO_3$ and STO [5]. On the other hand, it is important to understand the fundamental surface properties of the STO because similar considerations could be applied to other materials with similar structure [6]. The optical second harmonic generation (SHG) has emerged as a powerful experimental technique in recent decades to study the structural symmetry and electronic structure of materials due to the advantages of no requirement of the ultrahigh vacuum atmosphere and of high sensitivity to the surface and the interface [7–9]. Many interesting and significant properties, such as molecular adsorption, surface electric states, and magnetic domain structure, have been probed by this method [7,10–12]. Furthermore, the properties of many kinds of thin films epitaxially grown on the STO substrates have been studied by SHG method, such as the magnetic dead layer at the interface of $La_{0.6}Sr_{0.4}MnO_3$/STO [13] and the polar catastrophe [14] and the spatial inhomogeneity [15] at the $LaAlO_3$/STO interface. And some properties of the STO crystal also have been investigated using this method, such as the stress-induced ferroelectric [16] and near surface structure phase transition [17,18]. However, a systematical study on the second harmonic (SH) response from the STO surface has not been reported, which is important to understand the SH response of the various films, especially ultrathin films, grown on STO substrate. In addi-

*Corresponding author (email: kjjin@iphy.ac.cn)

tion, the perovskite manganites, which exhibits colossal magnetoresistance, have been widely researched due to their fascinating properties especially the unexpected phenomena coming from the surface and the interface of different heterostructures [19–22]. In this work, we have systematically investigated the second harmonic response of the STO surfaces and analyzed the surface symmetry of the (001)-oriented STO and (111)-oriented slightly Nb-doped STO crystals using SHG technique. The dependence of the second harmonic response on the sample's azimuthal angle and the polarization of the incident light have also been investigated. On the basis of the theoretical analysis, the conclusion is given that the surface symmetry of the STO (001) crystal is 4*mm*, and the surface of the Nb-doped (111) STO crystal possesses 3*m* symmetry. Furthermore, by modulating the surface of $La_{0.9}Sr_{0.1}MnO_3$ film with a capped STO layer, an enhancement of the surface polarization is exactly observed compared to that of bare $La_{0.9}Sr_{0.1}MnO_3$ film.

2 Experiments

Reflected SHG measurement has been adopted to probe the surface structure of STO crystal, and the experimental schematic of the reflected SHG setup is shown in Figure 1(a). A mode-lock femtosecond (fs) Ti:Sapphire oscillator (Tsunami 3941-X1BB, Spectra Physics) was employed to provide ~80 fs pulses at λ = 800 nm with the pulse repetition rate of 82 MHz. The fundamental light beam was focused onto the surface of sample with an incident angle of 45°. The second harmonic photons selected by the monochrometer on the reflected direction were detected and amplified by a photomultiplier tube and a preamplifier, respectively, and finally counted by a single-photon counter. A shortpass filter assigned in the reflection direction could filter the fundamental light (~800 nm) mixed with the SH radiation (~400 nm), while a longpass filter was used in the incident optical path to ensure that only the fundamental light could arrive to the sample's surface. A half-wave plate and a Glen-Taylor prism were used to select the fundamental and the SH light's polarization, respectively. The sample could be rotated along the normal direction of the sample's surface.

3 Physical models

As a second-order process, the SHG response is highly sensitive to the symmetry of the considered samples [23]. In general, considering the electric-dipole approximation, the bulk contribution of SHG would vanish in the medium with centrosymmetry. Therefore, the SH signals reflected by the surface of the materials only originate from the surface and/or interface where the broken inversion symmetry occurs [13,14,24]. For STO crystal, it has a cubic crystal structure with $Pm\bar{3}m$ space group including the inversion symmetry. The second-order response $\vec{\chi}^{(2)}$ always disappears in the bulk of the STO crystal, and then the SHG response only comes from the contribution of the surface.

The coordinate axes, the polarization geometry, and the definition of the azimuthal angle are shown in Figures 1(b) and 1(c), respectively. The intensity of SH radiation $I(2\omega)$ from the surface in the reflected geometry is [7,12]

$$I(2\omega) = \frac{2\omega^2}{\varepsilon_0 c^3 \cos^2\theta}\left|\chi_{eff}^{(2)}\right|^2 I_0^2(\omega). \quad (1)$$

In eq. (1), ω and $I_0(\omega)$ are the frequency and the intensity of the fundamental light, respectively. ε_0 and c are the permittivity and the speed of light in the vacuum, respectively. θ is the incident angle of the fundamental light. The effective surface second-order nonlinear susceptibility $\chi_{eff}^{(2)}$ is defined as [25]:

$$\chi_{eff}^{(2)} = [\vec{L}(2\omega)\cdot\hat{e}(2\omega)]\cdot\vec{\chi}_{surf}^{(2)} : [\vec{L}(\omega)\cdot\hat{e}(\omega)][\vec{L}(\omega)\cdot\hat{e}(\omega)], \quad (2)$$

where $\vec{\chi}_{surf}^{(2)}$ is the surface macroscopic second-order susceptibility tensor which has 3×3×3=27 elements. $\hat{e}(\omega)$ and $\hat{e}(2\omega)$ are the unit vectors of the electric field at ω and 2ω in air, respectively. $\vec{L}(\omega)$ and $\vec{L}(2\omega)$ are the transmission Fresnel tensors at ω and 2ω, respectively. $\vec{L}(\omega)$ has only three nonvanishing diagonal elements, i.e., $L_{xx}(\omega)$, $L_{yy}(\omega)$, and $L_{zz}(\omega)$ [25]. For a given experimental system, the components of $\vec{L}(\omega)$ are explicit and computable in mathematic expression, and $\vec{L}(2\omega)$ as well.

It is obvious that $\chi_{eff}^{(2)}$ contains all the information about the SHG measurements. And it can be rewritten as:

$$\chi_{eff}^{(2)} = [\vec{L}(2\omega)\cdot\hat{e}(2\omega)]\cdot\left[\frac{1}{\varepsilon_0 E_0^2}\vec{P}_{surf}(2\omega)\right],$$
$$\vec{P}_{surf}(2\omega) = \varepsilon_0\vec{\chi}_{surf}^{(2)} : [\vec{L}(\omega)\cdot\hat{e}(\omega)][\vec{L}(\omega)\cdot\hat{e}(\omega)]E_0^2. \quad (3)$$

$\vec{P}_{surf}(2\omega)$ is the 2nd-order surface dipole polarization density, and E_0 is the amplitude of the electric field of the incident light in air.

Supposing α is the polarization angle of the incident fundamental light, then we have

$$\hat{e}(\omega) = (\sin\alpha, \cos\alpha\cos\theta, \cos\alpha\sin\theta). \quad (4)$$

So if the material is specific, $\vec{\chi}_{surf}^{(2)}$ is explicit, and $\vec{P}_{surf}(2\omega)$ can be written in details.

Since slightly Nb-doped STO has the similar crystal structure with the STO crystal [26] except for strongly absorbing the fundamental and the second harmonic light, a Nb-doped (0.8 wt. %) STO (111) (SNTO) crystal was used to obtain the surface contribution signal in the SHG meas-

urement. The single crystals are one-side polished, and the roughness is less than 5 angstroms. Before probed, the crystals had been cleaned carefully by the ultrasonic cleaner sequentially using the analytic pure alcohol and the analytic pure acetone.

For the surface of STO (001) and SNTO (111) crystals, for simplicity, we assume that the surface has a simple unreconstructed structure, and then for a specified surface, its symmetry is the same as that of the bulk except for the direction perpendicular to the surface [27]. Therefore the symmetry of the surface of the STO (001) crystal is 4*mm* and that of the SNTO (111) surface is 3*m*. Consequently for the (001) surface, the susceptibility tensor $\ddot{\chi}^{(2)}_{surf}$ of 4*mm* symmetry has the form of [27,28]

$$\ddot{\chi}^{(2)}_{surf} = \begin{pmatrix} 0 & 0 & 0 & 0 & \chi_{xxz} & 0 \\ 0 & 0 & 0 & \chi_{xxz} & 0 & 0 \\ \chi_{zxx} & \chi_{zxx} & \chi_{zzz} & 0 & 0 & 0 \end{pmatrix}, \tag{5}$$

in the crystal principal coordinates, where $\chi_{ijk}(i,j,k\in\{x,y,z\})$ are constants.

Similarly, for the (111) surface, with the y axis perpendicular to the plane of symmetry, the tensor $\ddot{\chi}'^{(2)}_{surf}$ for 3*m* symmetry becomes [27,29]

$$\ddot{\chi}'^{(2)}_{surf} = \begin{pmatrix} \chi'_{xxx} & -\chi'_{xxx} & 0 & 0 & \chi'_{xxz} & 0 \\ 0 & 0 & 0 & \chi'_{xxz} & 0 & -\chi'_{xxx} \\ \chi'_{zxx} & \chi'_{zxx} & \chi'_{zzz} & 0 & 0 & 0 \end{pmatrix}. \tag{6}$$

It is important to point out that the components of the susceptibility, in general, are not the same for the different faces, i.e., $\chi^{(001)}_{ijk} \neq \chi^{(111)}_{ijk}$. A prime symbol is used for distinguishing them there.

Now if we express eqs. (5) and (6) in the $(\hat{x}, \hat{y}, \hat{z})$ coordinates shown in Figure 1(b) in terms of the rule of coordinate transformation of tensor, we have [27]

$$\ddot{\chi}'^{(2)}_{surf}(\varphi) = \begin{pmatrix} -\chi'_{xxx}\sin(3\varphi) & \chi'_{xxx}\sin(3\varphi) & 0 & 0 & \chi'_{xxz} & -\chi'_{xxx}\cos(3\varphi) \\ -\chi'_{xxx}\cos(3\varphi) & \chi'_{xxx}\cos(3\varphi) & \chi'_{xxz} & 0 & 0 & \chi'_{xxx}\sin(3\varphi) \\ \chi'_{zxx} & \chi'_{zxx} & \chi'_{zzz} & 0 & 0 & 0 \end{pmatrix}, \tag{7}$$

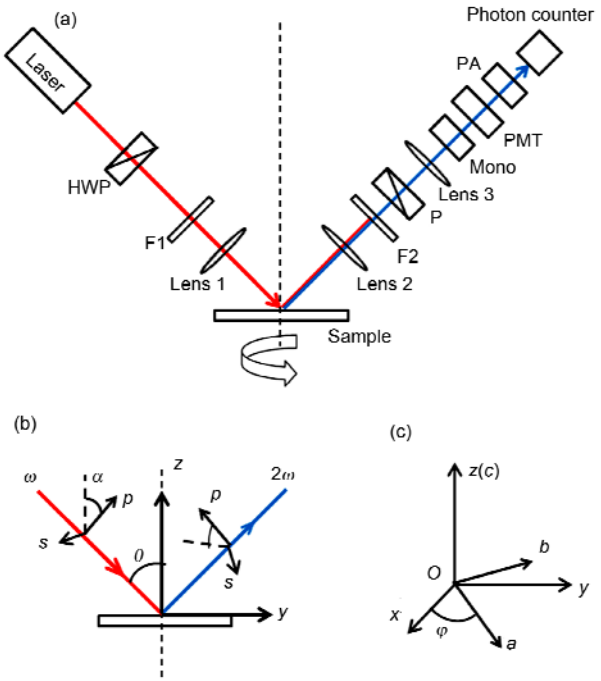

Figure 1 (Color Online) (a) The schematic of the reflected SHG setup. HWP: half-wave plate; P: Glen-Taylor prism; F1: longpass filter; F2: shortpass filter; Lens 1, Lens 2, and Lens 3: three plano-convex lenses; Mono: monochrometer; PMT: photomultiplier tube; PA: preamplifier. (b) The definition of coordinate axes and the polarization geometry. The angle θ and α denote the angle of incidence and the polarization angle of the fundamental light, respectively. (c) The definition of the azimuthal angle φ in the plane of the surface. The $(\hat{x}, \hat{y}, \hat{z})$ and $(\hat{a}, \hat{b}, \hat{c})$ denote the laboratory and crystal coordinate systems, respectively.

for (111) surface, and the tensor is the same as eq. (5), i.e., $\ddot{\chi}^{(2)}_{surf}(\varphi) = \ddot{\chi}^{(2)}_{surf}$ for (001) surface, where φ is the azimuthal angle of the sample on the plane of surface shown in the Figure 1(c).

Combining eqs. (3)–(7), we can express the theoretical SH intensity as follows: for the (001) surface, the SH intensity dependent on the polarization angle of the incident light for the two output polarizations (*p* and *s*) is

$$\begin{aligned} I_p(2\omega,\alpha) &= \frac{\omega^2}{4\varepsilon_0 c^3 \cos^2\theta} I_0^2(\omega)\left|\chi_{eff,\,p-out}\right|^2, \\ I_s(2\omega,\alpha) &= \frac{\omega^2}{\varepsilon_0 c^3 \cos^2\theta} I_0^2(\omega)\left|\chi_{eff,\,s-out}\right|^2. \end{aligned} \tag{8}$$

With the different combinations of the polarization, the azimuthal angle dependent SH intensity is

$$\begin{aligned} I_{pp}(2\omega) &= \frac{\omega^2}{4\varepsilon_0 c^3 \cos^2\theta} I_0^2(\omega)\left|\chi_{eff,pp}\right|^2, \\ I_{sp}(2\omega) &= \frac{\omega^2}{\varepsilon_0 c^3 \cos^2\theta} I_0^2(\omega)\left|\chi_{eff,sp}\right|^2, \\ I_{ps}(2\omega) &= 0. \end{aligned} \tag{9}$$

In eqs. (8) and (9), the definitions of *s*, *p*, and their combinations in the subscripts are given in Table 1. And the parameters of the effective susceptibility for the SH intensity are listed in Appendix.

For the SNTO (111) surface, similarly, the SH intensity

Table 1 The definitions of different polarization combinations of the input and output light. The polarizations are denoted by *p* (parallel to the plane of incidence) and *s* (perpendicular to the plane of incidence)

Polarization configuration		Notation
Input	Output	
p	*p*	*pp*
p	*s*	*ps*
s	*p*	*sp*
s	*s*	*ss*
Variable	*p*	*p*–out
Variable	*s*	*s*–out

dependence on the polarization α of the incident fundamental light for the *s* and *p* output polarizations can be expressed as:

$$I'_p(2\omega,\alpha)=\frac{\omega^2}{4\varepsilon_0 c^3\cos^2\theta}I_0^2(\omega)\left|\chi'_{eff,p-out}\right|^2,$$
$$I'_s(2\omega,\alpha)=\frac{\omega^2}{2\varepsilon_0 c^3\cos^2\theta}I_0^2(\omega)\left|\chi'_{eff,s-out}\right|^2. \quad (10)$$

And the SH intensity dependence on the azimuthal angle φ for different polarization combinations is

$$I'_{pp}(2\omega)=\frac{\omega^2}{4\varepsilon_0 c^3\cos^2\theta}I_0^2(\omega)\left|\chi'_{eff,pp}\right|^2,$$
$$I'_{sp}(2\omega)=\frac{\omega^2}{\varepsilon_0 c^3\cos^2\theta}I_0^2(\omega)\left|\chi'_{eff,sp}\right|^2,$$
$$I'_{ps}(2\omega)=\frac{\omega^2}{2\varepsilon_0 c^3\cos^2\theta}I_0^2(\omega)\left|\chi'_{eff,ps}\right|^2, \quad (11)$$
$$I'_{ss}(2\omega)=\frac{2\omega^2}{\varepsilon_0 c^3\cos^2\theta}I_0^2(\omega)\left|\chi'_{eff,ss}\right|^2.$$

The parameters of the effective susceptibility for the SNTO (111) surface are also listed in Appendix.

4 Results and discussion

The relationships between the SH signals and the azimuthal angle of the STO (001) surface are shown in Figure 2 for the polarization combinations of *pp*, *ps*, and *sp*. In addition, the linear fitting curves based on eq. (9) are also given. It can be seen from Figure 2, all measured curves are all almost flat, and show no variation with changing the rotation angle. And a good agreement between the theory and experiment is obtained. These results indicate that the contribution of the electric quadrupole and magnetic dipole of the STO bulk is negligible [27], and the electronic dipole approximation is applicable for the STO surfaces. Furthermore, it can be concluded that the symmetry of the STO (001) surface is 4*mm*. On the other hand, from the fact of $I_{ps}(2\omega)\simeq 0$ seen from Figure 2, it is confirmed that the measured SH signals only come from the surface, and the process of hyper-Rayleigh scatter is not remarkable [14,30].

Figures 3(a)–(d) show the polar plots of the azimuthal angle (φ)-dependent SH intensity with the polarization combinations of *pp*, *ps*, *sp*, and *ss* for the slightly doped SNTO (111) surface, respectively. It is obvious that a 3-fold symmetry is shown from the *pp* and *sp* curves, while a 6-fold symmetry is observed from the *ps* and *ss* curves. The behaviors of the SH response with respect to the sample's azimuth indicate a 3*m* symmetry for the SNTO (111) surface. In comfirming the crystal structure of the surface, the corresponding calculated curves based on eq. (11) are also plotted in Figure 3, and the fitting curves are in good agreement with the experimental data. These results verify that the symmetry of the SNTO (111) face is 3*m* with a 3-rotational axis perpendicular to the surface as expected above. Finally, it must be pointed out that the measured rotation angle in Figures 2 and 3 is not strictly consistent with the crystal azimuthal angle; a changeless deviation would be unavoidable because of the inconsistence between the specific crystal orientation and the laboratory coordinate axes. For further confirmation of the crystal structure of the SNTO (111) surface, the polarization-dependent SH measurements have been carried out at some certain azimuth angles (such as the positions of the maximum and minimum of the pp curve in Figure 3(a)). The dependences of the SH intensity of the *p*-out and *s*-out on the polarization α of the incident light are measured, respectively, and the theoretical intensity based on eq. (10) is also calculated. The good agreement between the experimental and theoretical results confirm the conclusions that the SNTO (111) surface has 3*m* symmetry.

Hole-doped perovskite manganese oxides, $Re_{1-x}A_xMnO_3$ (where Re = rare earth, A = alkaline earth), show fantastic properties remarkably affected by structural stress and external fields. $La_{0.9}Sr_{0.1}MnO_3/SrNb_{0.01}Ti_{0.99}O_3$ heterostructure constructed from epitaxial $La_{0.9}Sr_{0.1}MnO_3$ (LSMO) thin film,

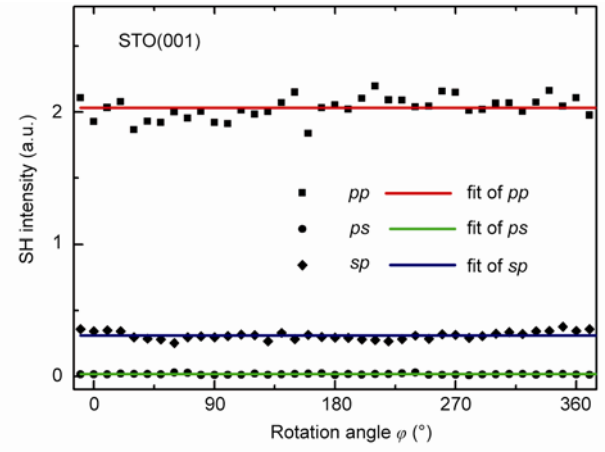

Figure 2 The SH intensity dependent on the rotation angle of the STO (001) crystal for different polarization combinations: *pp* (square), *ps* (circle), and *sp* (diamond); in addition, the theoretical fit curves are also plotted using color lines for *pp* (red), *ps* (green), and *sp* (blue).

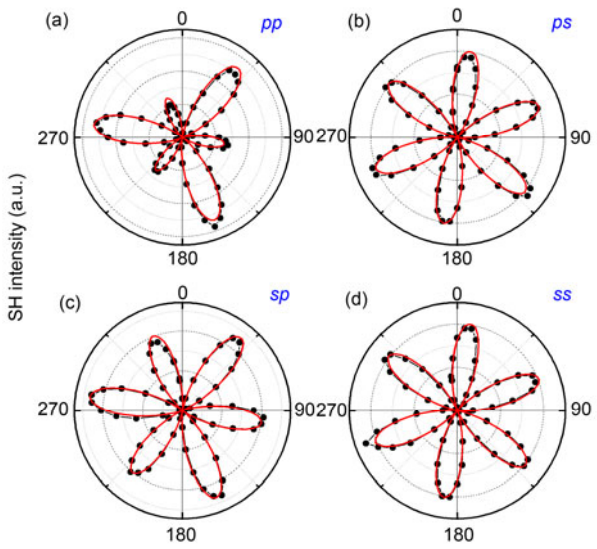

Figure 3 (Color Online) Polar plots of the SH intensity dependent on the rotation angle of the slightly Nb-doped STO (111) crystal for different polarization combinations. The black circle line curves and red line curves denote the experimental and theoretical data, respectively, for (a) *pp*, (b) *ps*, (c) *sp*, and (d) *ss*.

one of $Re_{1-x}A_xMnO_3$ compounds, on $SrNb_{0.01}Ti_{0.99}O_3$ substrate, exhibits the positive magnetoresistance [31], the ultrafast photoelectric effect [32,33], and the transient lateral photovoltage [34]. All of these properties are believed to be related to the surface and/or the interface of these heterostructures, thus it is important to investigate the characteristics of the surface/interface of the heterojunctions for further understanding those effects. The surface of the LSMO film synthesized on the STO (001) substrate has the similar symmetry to the surface of STO (001). To investigate the surface modulation, we fabricated the LSMO thin films and the STO layer-capped LSMO thin films on the STO (001) substrates grown by laser molecular beam epitaxy (Laser-MBE). The LSMO layer is as thick as 400 unit cells (u.c.), and the thickness of the capped STO layer is 50 u.c.. The detailed growth can be found in our previous work [20,33,35]. The results of x-ray diffraction and in-situ reflected high energy electron diffraction reveal that the films have grown along *c*-axis with good single phase.

In the reflected SHG measurements, the contributions from the interface between the LSMO film and the substrate are negligibly small (<5‰), because the optical absorption coefficient in the LSMO films [13] is large enough for both the fundamental light (λ = 800 nm) and SH light (λ = 400 nm). The SH signals detected come from the surface of LSMO or the STO-modulated surface of LSMO, and the schematic of light path can be seen in the inset in Figure 4. The SH intensities dependent on the polarization of the fundamental light are shown in Figures 4(a) and 4(b) for the LSMO and STO/LSMO films, and the signals from the surface of STO substrate are also plotted in Figure 4 for comparison. The SH intensity curves in Figure 4 could be well fitted based on eq. (8). The difference of the data originated between the LSMO and STO/LSMO films are clearly seen in the *p*-out and *s*-out plots. Especially the effective 2nd-order nonlinear susceptibility for *sp* polarization combination $\chi_{eff,\,sp}$, which is proportional to the square root of the SH intensity denoted by a vertical violet dash line in Figure 4 (a), has been remarkably more enhanced for the interface STO-modulated LSMO film than that of the LSMO film. Observed from Appendix, the component $\chi_{eff,\,sp}$ is proportional to χ_{zxx}, which reflects the polarization characteristics derived from in-plane crystal structure, so the enhanced surface polarization indicates the modulation of the in-plane crystal structure of the LSMO's surface by the STO capped layer. Similar enhancement is also observed in Figure 4(b), which is related to the susceptibility element χ_{xxz} concluded from eq. (8). Compared to the data originated from the STO substrate, although the SH signal from STO/LSMO is the interference of the signals coming from the surface of STO film and the STO/LSMO interface, we believe that the contribution from the interface is dominant because the signal from the surface of STO film is very

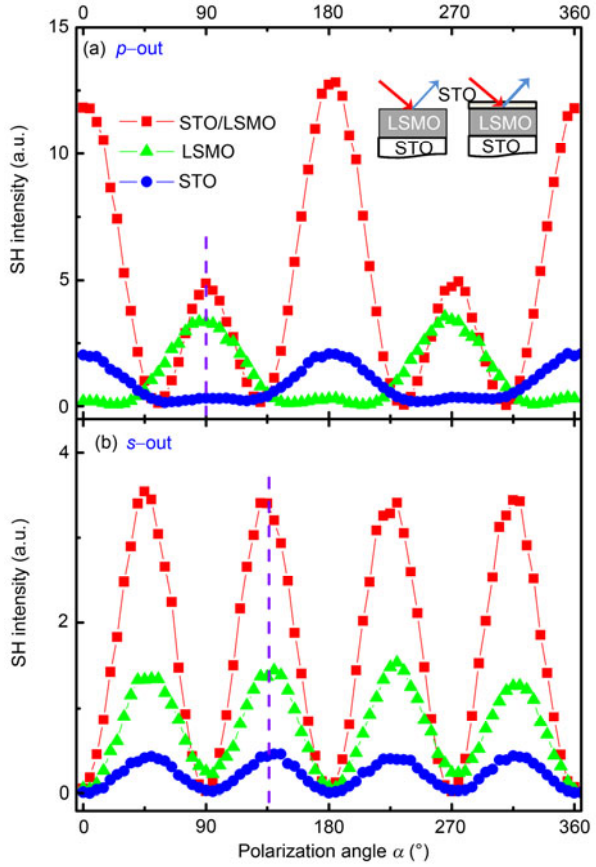

Figure 4 (Color Online) (a) *p*–out and (b) *s*–out SH intensity dependence on the polarization angle (α) of the fundamental light for STO/LSMO film (red square line), LSMO film (green triangle line), and STO substrate (blue circle line), respectively. The vertical violet dash lines denote the SH intensity of *sp* combination in (a) and of the peaks of the *s*-out curves in (b). The inset shows the schematic setups for the different LSMO structures.

smaller than the former. We consider the capped STO layer as surface modulation for the LSMO film for simplicity. Thus it is clearly seen that the surface polarization property of the LSMO film can be remarkably enhanced by modulated LSMO surface using the STO capped layer.

5 Conclusions

In the present study, the crystal structure of the different surfaces of the STO crystal was investigated by using the reflected optical SHG technique. The SH radiation only originates from the surfaces of the STO crystal due to the inversion symmetry of the bulk. The good consistency between the azimuth-dependent SH intensity curves and theoretical curves indicates that the STO (001) surface has 4*mm* symmetry, and the SNTO (111) surface shows 3*m* symmetry. The results of polarization-dependent measurement further confirm our conclusion. The surface polarization can be exactly detected by the SHG method and would be enhanced by modulating the surface of LSMO films with a STO capped layer.

Appendix Parameters for the SH intensity of the STO (001) and SNTO (111) surfaces.

(001)

$\chi_{eff,pp}$ $\chi_{zxx}(L_{yy}^{\omega})^2 L_{zz}^{2\omega} + \chi_{zzz}(L_{zz}^{\omega})^2 L_{zz}^{2\omega} - \sqrt{2}\chi_{xxz} L_{yy}^{\omega} L_{zz}^{\omega} L_{yy}^{2\omega}$

$\chi_{eff,sp}$ $\chi_{zxx}(L_{xx}^{\omega})^2 L_{zz}^{2\omega}$

$\chi_{eff,p-out}$ $\left[\chi_{zxx}(L_{yy}^{\omega})^2 L_{zz}^{2\omega} + \chi_{zzz}(L_{zz}^{\omega})^2 L_{zz}^{2\omega} - \sqrt{2}\chi_{xxz} L_{yy}^{\omega} L_{zz}^{\omega} L_{yy}^{2\omega}\right]\cos^2\alpha + 2\chi_{zxx}(L_{xx}^{\omega})^2 L_{zz}^{2\omega}\sin^2\alpha$

$\chi_{eff,s-out}$ $\chi_{xxz} L_{xx}^{\omega} L_{zz}^{\omega} L_{xx}^{2\omega}\sin 2\alpha$

(111)

$\chi'_{eff,pp}$ $-\chi'_{xxx}(L_{yy}^{\omega})^2 L_{yy}^{2\omega}\cos 3\varphi + \left[\chi'_{zxx}(L_{yy}^{\omega})^2 L_{zz}^{2\omega} + \chi'_{zzz}(L_{zz}^{\omega})^2 L_{zz}^{2\omega} - \chi'_{xxz}(L_{zz}^{\omega})^2 L_{yy}^{2\omega}\right]$

$\chi'_{eff,sp}$ $\chi'_{xxx}(L_{xx}^{\omega})^2 L_{yy}^{2\omega}\cos 3\varphi + \chi'_{zxx}(L_{xx}^{\omega})^2 L_{zz}^{2\omega}$

$\chi'_{eff,ps}$ $\chi'_{xxx}(L_{yy}^{\omega})^2 L_{xx}^{2\omega}\sin 3\varphi$

$\chi'_{eff,ss}$ $-\chi'_{xxx}(L_{xx}^{\omega})^2 L_{xx}^{2\omega}\sin 3\varphi$

$\chi'_{eff,p-out}$ $\left[2\chi'_{xxx}(L_{xx}^{\omega})^2 L_{yy}^{2\omega}\sin^2\alpha - \chi'_{xxx}(L_{yy}^{\omega})^2 L_{yy}^{2\omega}\cos^2\alpha\right]\cos 3\varphi - \left(\sqrt{2}\chi'_{xxx} L_{xx}^{\omega} L_{yy}^{\omega} L_{yy}^{2\omega}\sin 2\alpha\right)\sin 3\varphi$
$+\left[2\chi'_{zxx}(L_{xx}^{\omega})^2 L_{zz}^{2\omega}\sin^2\alpha + \chi'_{zxx}(L_{yy}^{\omega})^2 L_{zz}^{2\omega}\cos^2\alpha + \chi'_{zzz}(L_{zz}^{\omega})^2 L_{zz}^{2\omega}\cos^2\alpha - \chi'_{xxz}(L_{zz}^{\omega})^2 L_{yy}^{2\omega}\cos^2\alpha\right]$

$\chi'_{eff,s-out}$ $\left[\chi'_{xxx}(L_{yy}^{\omega})^2 L_{xx}^{2\omega}\cos^2\alpha - 2\chi'_{xxx}(L_{xx}^{\omega})^2 L_{xx}^{2\omega}\sin^2\alpha\right]\sin 3\varphi - \left(\sqrt{2}\chi'_{xxx} L_{xx}^{\omega} L_{yy}^{\omega} L_{xx}^{2\omega}\sin 2\alpha\right)\cos 3\varphi$
$+\sqrt{2}\chi'_{xxz} L_{xx}^{\omega} L_{zz}^{\omega} L_{xx}^{2\omega}\sin 2\alpha$

This work was supported by the National Basic Research Program of China (Grant Nos. 2012CB921403 and 2013CB328706) and the National Natural Science Foundation of China (Grant No. 11134012).

1 Reyren N, Thiel S, Caviglia A D, et al. Superconducting interfaces between insulating oxides. Science, 2007, 317: 1196–1199
2 Mannhart J, Schlom D G. Oxide interfaces–an opportunity for electronics. Science, 2010, 327: 1607–1611
3 Bhattacharya A, May S J, te Velthuis S G E, et al. Metal-insulator transition and its relation to magnetic structure in $(LaMnO_3)_{2n}$/$(SrMnO_3)_n$ superlattices. Phys Rev Lett, 2008, 100: 257203
4 Herger R, Willmott P R, Bunk O, et al. Surface structure of $SrTiO_3$ (001). Phys Rev B, 2007, 76: 195435
5 Ohtomo A, Hwang H Y. A high-mobility electron gas at the $LaAlO_3/SrTiO_3$ heterointerface. Nature, 2004, 427: 423–426
6 Erdman N, Poeppelmeier K R, Asta M, et al. The structure and chemistry of the TiO_2-rich surface of $SrTiO_3$ (001). Nature, 2002, 419: 55–58
7 Shen Y R. Surface properties probed by second-harmonic and sum-frequency generation. Nature, 1989, 337: 519–525
8 Miyauchi Y, Sano H, Okada J, et al. Simultaneous optical second harmonic and sum frequency intensity image observation of hydrogen deficiency on a H–Si (111) 1×1 surface after IR light pulse irradiation. Surf Sci, 2009, 603: 2972–2977
9 Kirilyuk A, Rasing T. Magnetization-induced-second-harmonic generation from surfaces and interfaces. J Opt Soc Am B, 2005, 22: 148–167
10 McGilp J F. Probing surface and interface structure using optics. J Phys Condens Matter, 2010, 22: 084018
11 Fiebig M, Pavlov V V, Pisarev R V. Second-harmonic generation as a tool for studying electronic and magnetic structures of crystals: Review. J Opt Soc Am B, 2005, 22: 96–118
12 Gielis J J H, Gevers P M, Aarts I M P, et al. Optical second-harmonic generation in thin film systems. J Vac Sci Technol A, 2008, 26: 1519–1537
13 Yamada H, Ogawa Y, Ishii Y, et al. Engineered interface of magnetic oxides. Science, 2004, 305: 646–648
14 Savoia A, Paparo D, Perna P, et al. Polar catastrophe and electronic reconstructions at the $LaAlO_3/SrTiO_3$ interface: Evidence from optical second harmonic generation. Phys Rev B, 2009, 80: 075110
15 Günter T, Rubano A, Paparo D, et al. Spatial inhomogeneities at the $LaAlO_3/SrTiO_3$ interface: Evidence from second harmonic generation. Phys Rev B, 2012, 86: 235418
16 Fujii Y, Uwe H, Sakudo T. Stress-induced quantum ferroelectricity in $SrTiO_3$. J Phys Soc Jpn, 1987, 56: 1940–1942
17 Uesu Y, Nakai R, Kato N, et al. SHG microscopic studies on low temperature phase transitions of $SrTi^{16}O_3$ and $SrTi^{18}O_3$. Ferroelectrics,

2003, 285: 19–26
18 Mishina E D, Misuryaev T V, Sherstyuk N E, et al. Observation of a near-surface structural phase transition in $SrTiO_3$ by optical second harmonic generation. Phys Rev Lett, 2000, 85: 3664–3667
19 Tokura Y. Critical features of colossal magnetoresistive manganites. Rep Prog Phys, 2006, 69: 797–851
20 Jin K J, Lu H B, Zhao K, et al. Novel multifunctional properties induced by interface effects in perovskite oxide heterostructures. Adv Mater, 2009, 21: 4636–4640
21 Yang J, Sun Y P. Study of doping effect, phase separation and heterojunction in CMR manganites. Sci China-Phys Mech Astron, 2013, 56: 85–98
22 Huang Y H, Lu H B, He M, et al. Nanosecond photoelectric effects in all-oxide p-n junction of $La_{0.9}Sr_{0.1}MnO_3/SrNb_{0.01}Ti_{0.99}O_3$. Sci China Ser G-Phys Mech Astron, 2005, 48: 381–384
23 Shen Y R. Surface second harmonic generation: A new technique for surface studies. Annu Rev Mater Sci, 1986, 16: 69–86
24 Guyot-Sionnest P, Chen W, Shen Y R. General consideration on optical second-harmonic generation from surfaces and interfaces. Phys Rev B, 1986, 33: 8254–8263
25 Rao Y, Tao Y S, Wang H F. Quantitative analysis of orientational order in the molecular monolayer by surface second harmonic generation. J Chem Phys, 2003, 119: 5226–5236
26 Maegli A, Yoon S, Otal E, et al. Perovskite-type $SrTi_{1-x}Nb_x(O,N)_3$ compounds: Synthesis, crystal structure and optical properties. J Solid State Chem, 2011, 184: 929–936
27 Sipe J E, Moss D J, van Driel H M. Phenomenological theory of optical second- and third-harmonic generation from cubic centrosymmetric crystals. Phys Rev B, 1987, 35: 1129–1141
28 Tom H W K, Heinz T F, Shen Y R. Second-harmonic refelection from silicon surfaces and its relation to structural symmetry. Phys Rev Lett, 1983, 51: 1983–1986
29 Liu C W, Chang S J, Liu C C, et al. Inspecting the surface of implanted Si(111) during annealing by reflective second harmonic generation: The influence of chamber pressure. Thin Solid Films, 2013, 529: 282–286
30 David B H. Review of hyper-rayleigh and second-harmonic scattering in minerals and other inorganic solids. Am Mineral, 1988, 73: 701–706
31 Jin K J, Lu H B, Zhou Q L, et al. Positive colossal magnetoresistance from interface effect in p-n junction of $La_{0.9}Sr_{0.1}MnO_3$ and $SrNb_{0.01}Ti_{0.99}O_3$. Phys Rev B, 2005, 71: 184428
32 Huang Y H, Jin K J, Zhao K, et al. Photoelectric characteristic of $La_{0.9}Sr_{0.1}MnO_3$ and $SrNb_{0.01}Ti_{0.99}O_3$ p-n heterojunctions. Chin Phys Lett, 2006, 23: 982–985
33 Wang C, Jin K J, Zhao R Q, et al. Ultimate photovoltage in perovskite oxide heterostructures with critical film thickness. Appl Phys Lett, 2011, 98: 181101
34 Jin K J, Zhao K, Lu H B, et al. Dember effect induced photovoltage in perovskite p-n heterojunctions. Appl Phys Lett, 2007, 91: 081906
35 Lu H B, Dai S Y, Chen Z H, et al. High sensitivity of positive magnetoresistance in low magnetic field in perovskite oxide p–n junctions. Appl Phys Lett, 2005, 86: 032502